RSC Advances

PAPER

View Article Online
View Journal | View Issue

Cite this: *RSC Adv.*, 2020, **10**, 8115

Organic template-assisted green synthesis of $CoMoO_4$ nanomaterials for the investigation of energy storage properties†

Irum Shaheen,[a] Khuram Shahzad Ahmad, *[a] Camila Zequine,[b] Ram K. Gupta,[b] Andrew Thomas[c] and Mohammad Azad Malik[c]

Transitional metal oxide nanomaterials are considered to be potential electrode materials for supercapacitors. Therefore, in the past few decades, huge efforts have been devoted towards the sustainable synthesis of metal oxide nanomaterials. Herein, we report a synergistic approach to synthesize spherical-shaped $CoMoO_4$ electrode materials using an inorganic–organic template *via* the hydrothermal route. As per the synthesis strategy, the precursor solution was reacted with the organic compounds of *E. cognata* to tailor the surface chemistry and morphology of $CoMoO_4$ by organic species. The modified $CoMoO_4$ nanomaterials revealed a particle size of 23 nm by X-ray diffraction. Furthermore, the synthesized material was scrutinized by Fourier transform infrared spectroscopy, X-ray photoelectron spectroscopy, field emission scanning electron microscopy and energy dispersive spectroscopy. The optical band gap energy of 3.6 eV was calculated by a Tauc plot. Gas chromatography-mass spectrometry identified cyclobutanol (C_4H_8O) and octodrine ($C_8H_{19}N$) as the major stabilizing agents of the $CoMoO_4$ nanomaterial. Finally, it was revealed that the bioorganic framework-derived $CoMoO_4$ electrode exhibited a capacitance of 294 F g^{-1} by cyclic voltammetry with a maximum energy density of 7.3 W h kg^{-1} and power density of 7227.525 W kg^{-1}. Consequently, the nanofeatures and organic compounds of *E. cognata* were found to enhance the electrochemical behaviour of the $CoMoO_4$-fabricated electrode towards supercapacitor applications.

Received 13th November 2019
Accepted 14th January 2020

DOI: 10.1039/c9ra09477f

rsc.li/rsc-advances

1. Introduction

One key challenge of the present time is the increasing demand of energy storage devices to store renewable energies.[1–6] Among such storage systems, supercapacitors (SCs) are the candidates with the most potential owing to their high power density in energy storage devices.[5–7] The SCs can efficiently and sustainably fulfill the demands of energy storage as compared to batteries, which are generally of low power density.[7–10] SCs are of different types depending on the nature of the electrode material,[1,6,9,15–18] and their performances are critically reliant on their electrode material.[6,9,15–18] Therefore, in order to achieve high SC performance, an efficient way is to develop electrode materials with tailored and enhanced morphology.[19,20] Over recent years, transition metal oxides have been widely investigated as electrode materials.[3,6,9–18] The notable advantages of using metal oxides as electrode materials are earth abundance, high theoretical capacity, economical use and ability to be modified in different morphologies and structures.[9–14] In particular, constructing and modifying the morphologies as well as the surface chemistry of the metal oxides at the nanoscale level have been highly investigated among the scientific community.[8–15] The modified nanostructures of transition metal oxides with carbon and oxygen-containing surface functional groups have greatly enhanced the electrochemical performance of SCs.[10–14] Nevertheless, the synthesis of metal oxide nanomaterials with modified surface chemistry has certain limitations such as high cost, large-scale production, sophisticated techniques and complicated synthesis procedures.[1,6,7,9,20] Thus, the sustainable synthesis of metal oxide nanomaterials with effective functional groups is still a great challenge in the 21st century.[45,48,51,54,59]

In this regard, herein, we developed a sustainable synthesis route to synthesize metal oxide nanostructures ($CoMoO_4$) *via* an inorganic–organic framework. *Euphorbia cognata* Boiss has been used as a source of organic compounds for the first time. The Euphorbiaceae species are reported to have phytochemicals such as diterpenoids, tannins, flavonoids, taraxerol, terpenoids, lectins, cycloartenol, alkaloids, and neriifolins.[74,75] These phytochemicals have been extensively used as reducing and capping agents in the

[a]*Department of Environmental Sciences, Fatima Jinnah Women University, Rawalpindi, Pakistan. E-mail: chemist.phd33@yahoo.com; dr.k.s.ahmad@fjwu.edu.pk*

[b]*Department of Chemistry, Pittsburg State University, 1701 South Broadway Street, Pittsburg, KS 66762, USA*

[c]*Department of Materials, Photon Science Institute, Sir Henry Royce Institute, Alan Turing Building, The University of Manchester, Oxford Road, Manchester M13 9PL, UK*

† Electronic supplementary information (ESI) available. See DOI: 10.1039/c9ra09477f

synthesis of nanoparticles.[23–28] However, these studies lack an in-depth mechanism and have been unable to identify the incorporated bioactive compounds in the synthesized nanomaterials. Moreover, the reported plant-mediated synthesis is often limited to the mono metal oxides. Therefore, we were motivated to investigate *E. cognata* for the synthesis of $CoMoO_4$ nanocomposites for the first time. First of all, we have analyzed and identified the organic compounds of the respective plant leaves (shown in S1, S2 and S3†). It revealed different phenolic compounds such as decanoic acid, octodrine, cyclobutanol, D-alanine, and cyclohexylethylamine. Synthetic D-alanine, decanoic acid, and cylcobutanal have been used as fuel and reducing agents in the synthesis of nanomaterials in a number of studies.[21,22,71–73] Therefore, the selection of the plant was made on the basis of its significant phytoconstituents that could be used as reducing and stabilizing agents in the synthesis of nanomaterials. Furthermore, to the best of our knowledge, *E. cognata* has not been previously investigated for the synthesis of nanomaterials.

Plant phytochemicals have been reported as reducing (as well as capping) agents in the synthesis of nanoparticles.[23–28] Thus, we believed that *E. cognata* would induce carbon, oxygen and N-containing organic compounds in the synthesized material. Previously, metal oxides with carbon nanotubes, graphene, and carbon black have been investigated as an outstanding approach for acquiring carbon and oxygen-containing surface functional groups to improve the conductivity and capacitance of the capacitor.[10,11,15,16,19,20] Here, we have tailored the surface chemistry of $CoMoO_4$ to introduce C, H, O, N-related functional groups *via* organic species of *E. cognata*. We believe that when such functional groups are introduced in the metal oxide nanomaterials, their electronic structure and morphology will be changed, which will create more active sites and quick diffusion pathways. This will lead to better electrical conductivity and an improved redox behaviour of the SC electrode.

2. Materials and methods

Molybdenum(II) acetate ($Mo_2(O_2CCH_3)_4$), cobalt(II) acetate tetrahydrate ($C_4H_6CoO_4 \cdot 4H_2O$), ethanol (C_2H_5OH), methanol (CH_3OH), ethylene glycol (C_2H_6O2) and citric acid ($C_6H_8O_7$) were purchased from Merck Chemicals, Ltd. Double-distilled and deionized water was used throughout the experiment. The phytochemical extract of *E. cognata* plant leaves was used as reducing and stabilizing agents in the synthesis of $CoMoO_4$ and was sampled from Rawalakot AJK Pakistan. Acetylene black, polyvinylidenedifluoride (PVDF) and *N*-methyl pyrrolidinone (NMP) were used in the fabrication of the electrode.

2.1. Synthesis of $CoMoO_4$

The organic–inorganic framework-based strategy to synthesize $CoMoO_4$ nanomaterials (Fig. 1) was developed by modifying reported methodologies, particularly relating to metal–organic frameworks (MOFs).[19,20,23–28,59,60] 250 ml of 20 mM aqueous solutions of $C_4H_6CoO_4 \cdot 4H_2O$ and $Mo_2(O_2CCH_3)_4$ were prepared separately in deionized water. Each solution was subjected to constant magnetic stirring at room temperature until complete dissolution was achieved; afterwards, both solutions were mixed together. In another beaker, 2 g of dried powdered leaves of *E. cognata* were treated with deionized water on vigorous stirring for 30 minutes at 60 °C to extract organic compounds. After 30 minutes, the extract was cooled down at room temperature and then filtered through Whatman filter paper. Hereinto, 20 ml of the plant organic complex was added into a mixed solution of the precursor on continuous stirring at 70 °C for 2 h, and then incubated at room temperature under dark conditions for 24 hours to attain the phyto-functional groups, and to complete the hydrolysis and precipitation process. Hereafter, the mixture of inorganic metal precursors and organic species of *E. cognata* was first evaporated at 95 °C overnight. The dried powder was then annealed at 450 °C for 4 hours to procure the $CoMoO_4$ nanomaterial.

The thermally annealed $CoMoO_4$ nanomaterial was mixed with acetylene black and polyvinylidenedifluoride (PVDF) in an 8 : 1 : 1 ratio in the presence of *N*-methyl pyrrolidinone (NMP) following reported methodologies.[29–32] The prepared slurry was then consistently pasted onto the

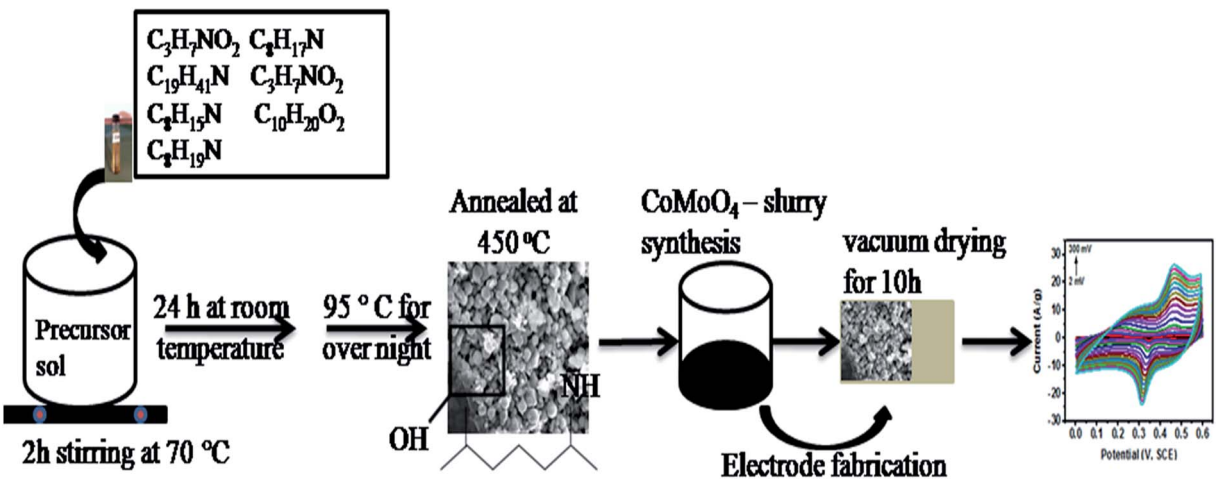

Fig. 1 Schematic diagram of the modified hydrothermal method *via* organic compounds to synthesize $CoMoO_4$ for fabrication of the electrode.

porous Ni foam and dried at 60 °C under vacuum for 10 h. The mass loading was accurately measured by weighing the nickel foam before and after electrode preparation using an analytical balance.

3. Characterization

The functionalized $CoMoO_4$ was well characterized by ultraviolet-visible spectroscopy (UV-Vis, spectrophotometer 1602, Biomedical services, Spain) for band gap and optical properties. Phyto-stabilizing agents were analyzed by gas chromatography-mass spectroscopy (GC-MS-QP5050, SHIMADZU) and Fourier transforms infrared spectroscopy (FTIR, 8400, Shimadzu, Japan). The phase identification and crystallinity were examined by an XRD5 PANalytical X'Pert Pro. A Quanta 250-FEG scanning electron microscope (FE-SEM) with a Gatan 3View attachment was used to study the morphology and energy-dispersive X-ray spectroscopy (EDX) was used to study the chemical composition of the synthesized $CoMoO_4$. The surface chemistry was investigated by X-ray photoelectron spectroscopy (XPS) using a Kratos Axis Ultra spectrometer with a monochromated Al Kα X-ray source.

3.1. Electrochemical measurements

Electrochemical characterizations of the organic compound stabilized $CoMoO_4$ were carried out using the three-electrode system, where fabricated nickel foam with $CoMoO_4$ was used as the working electrode, a platinum wire was used as the counter electrode and a saturated calomel electrode was used as the reference electrode. All experiments were conducted in 3 M KOH aqueous solution. The electrochemical properties of $CoMoO_4$ were investigated by cyclic voltammetry (CV) at various scan rates (2 to 300 mV s^{-1}), galvanostatic charge–discharge (GCD) at various current densities (0.5–30 A g^{-1}) and electrochemical impedance spectroscopy (EIS) with a frequency range of 50 mHz to 10 kHz.

4. Results and discussion

4.1. Phyto-functionalized $CoMoO_4$ nanomaterial

In order to identify the bioactive organic compounds of the plant extract, the spectroscopic characterization of a prepared extract of *E. cognata* leaves was carried out and revealed the distinctive peaks as shown in S1,† Fig. 1b. The identified peaks in the ultraviolet and visible regions correspond to plant

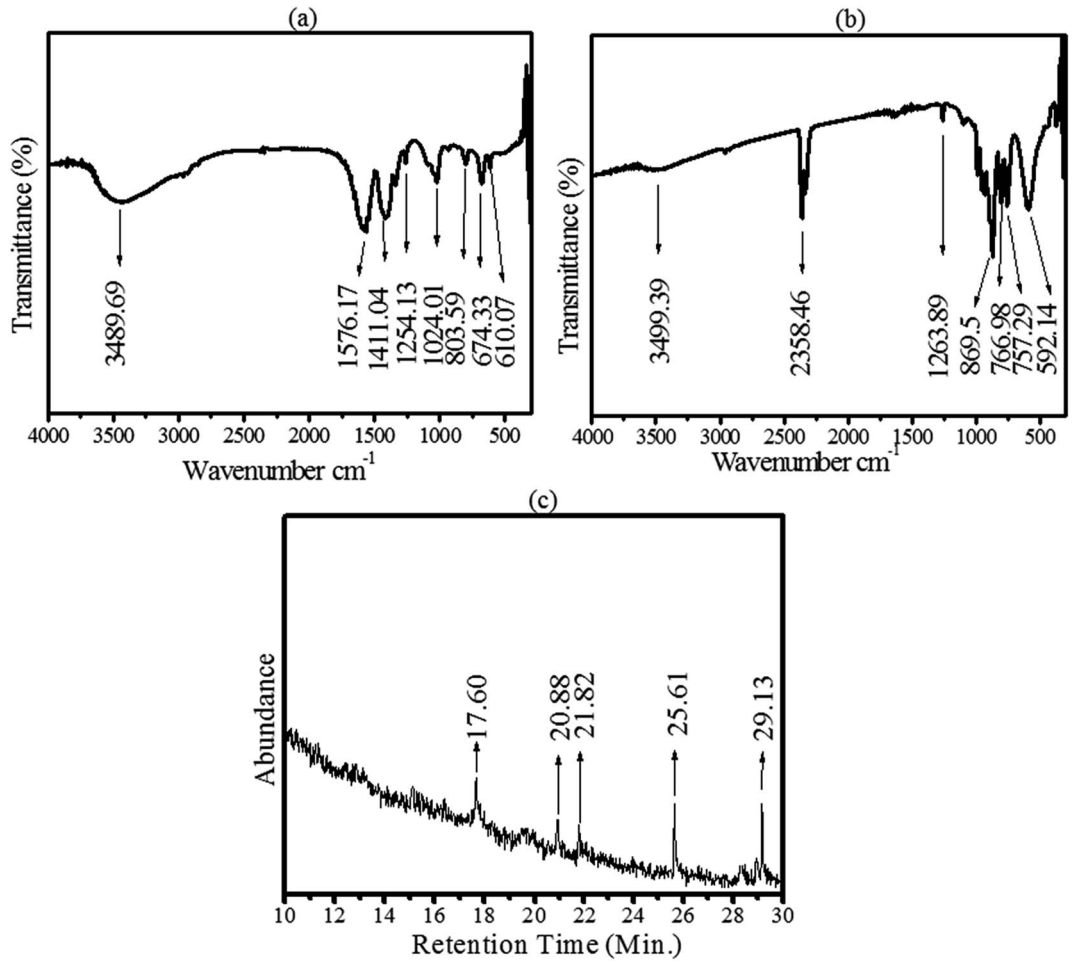

Fig. 2 Identification of organic stabilizing agents of $CoMoO_4$. (a) FTIR spectra of $CoMoO_4$ after drying at 95 °C. (b) FTIR of $CoMoO_4$ after annealing at 450 °C, and (c) GC-MS spectra of $CoMoO_4$.

Table 1 Functional groups of organic compounds of $CoMoO_4$ identified by recorded peak frequencies *via* FTIR[a]

Peaks (cm^{-1}) after oven drying	Peaks (cm^{-1}) of annealed sample	Bond	Assignments	Functional groups
3489.69	3499.39	O–H	υ	Plant phenolic compounds[23,24]
	2358.46	C≡N	υ	Nitrile compounds of *E. cognata*[23,26]
1576.17		C–C (in ring)	υ	Aromatic ring of phenol and flavonoids of *E. cognata*[24–26]
1411.04		C–C (ring)	υ	Phenolic compounds of the plant[23–26]
1254.13	1263.89	C–O	υ	Phenol and carboxylic acids of the plant leaves[26]
1024.01		C–N	υ	Plant amines groups of phytocompounds such as $C_8H_{19}N$[25,26]
803.59	869.5	=C–H	δ	Hydrocarbon (unsaturated)[24–26]
	766.98	C–H	ρ	Alkane (saturated hydrocarbon) from *E. cognata* phytochemicals[23–25]
	757.29	C–H	ρ	Alkane (paraffin) saturated hydrocarbon of the leaves extract[24–26]
674.33		N–H	ω	1°, 2° amines of plant phenols[24]
610.07		–C≡C–H:C–H	δ	Unsaturated hydrocarbon such as alkynes[23–26]
	529.14	C–M, M–O	υ	Metal oxides (Co–O, Mo–O)[23–26]

[a] υ = stretching, δ = bending, ρ = rocking, ω = wagging.

phenols, as well as flavonoids comprising a benzene ring with the conjugation of ring A and its configurations. The absorbance values at 297.31 nm and 337.81 nm suggest the presence of plant flavonoids having conjugation of rings B and C. The additional absorption bands at 364.10 and 385.96 nm are indicative of flavones and flavonols in the plant extract.[33]

The dried powdered leaves of *E. cognata* were subjected to scan at the full frequency range (400 to 4000 cm^{-1}) of FTIR (Fig. 1a, S1†). FTIR illustrated the vibration modes associated with phytochemicals at frequencies (cm^{-1}): 3417.98 (O–H stretching and H bond), 2962.76 (C–H), 2918.40 (C–H), 1639.55 (N–H and –C=C–), 1417.73 (C–C medium stretch (in ring)), 1261.49 (C–H wag (–CH_2X) bond, C–N and C–O), 1097.53 (C–N stretch), 1024.24 (C–N stretch), 864.14 (=C–H, N–H wag and C–H oop), 800.49 (=C–H, N–H wag and C–H oop) and 536.2 (C–Br). Therefore, in agreement with the UV analysis of the leaves, the FTIR studies illustrated the alcohol, phenol, aromatic, alkanes, 1° and 2° amines, aliphatic amines, carboxylic acid, esters and ether groups as the organic constituents of the investigated plant leaves.

In order to confirm the possible role of the organic compounds of *E. cognata* in the synthesis of the nanomaterials, a $CoMoO_4$ pellet was first dried at 95 °C and revealed the presence of associated phytochemicals, as shown in Fig. 2a. Afterwards, $CoMoO_4$ was annealed at 450 °C and subjected to FTIR to identify the functional groups of the incorporated bioactive compounds, as depicted in Fig. 2b. Fig. 2b revealed the presence of a Mo[6] and Co[34,35] metal bond in the fingerprint region (500 to 400 cm^{-1}), along with major organic compounds of the *E. cognata* leaves as part of the reducing and stabilizing agents of $CoMoO_4$. Table 1 further explains the organic groups of $CoMoO_4$ corresponding to alcohol and phenol, aldehydes, ester, saturated aliphatics, nitro-compounds (N–O), aliphatic amines, carboxylic acid (O–H bend) and 1°, 2° amines, in agreement with the reported literature.[23–26] It is worth noting that after calcinations, vibration peaks at 1576.17 cm^{-1}, 1411.04 cm^{-1}, 674.33 cm^{-1} and 610.07 cm^{-1} seemed to disappear (Table 1, Fig. 2b). This is possibly because of the fact that at higher temperatures (450 °C), some organic compounds were degraded/transformed into their metabolites. However, after the annealing process, alcohol, phenol, aldehydes, saturated aliphatics and carboxylic acid were found to be present in the synthesized nanomaterial as stabilizing agents, while a vibrational frequency appeared at 521.12 cm^{-1} corresponding to the M–O and M–C bonds (M = Co and Mo).

The organic stabilizing agents were further characterized by GC-MS. The results pertaining to the GC-MS analysis of a methanolic extract of *E. cognata* identified numerous compounds at their particular retention times (as shown in the annotated mass spectra on S1,† Fig. 3, Table 1, S2 and S3 in the ESI†). The GC-MS profile of *E. cognata* leaves revealed the presence of octodrine, alanine, cyclobutanol, decanoic acid, azabicyclo, 2-aminodecane and cyclohexylethylamine, as shown in Fig. 1. These bioactive compounds as stabilizing agents were identified in the methanolic suspension of the $CoMoO_4$ nanocomposite as shown in Fig. 2c. The identified peaks in Fig. 2c correspond to cyclobutanol (C_4H_8O) and octodrine ($C_8H_{19}N$), according to the GC-MS profiling of the NIST library. Therefore, GCMS endorsed the functionalization of $CoMoO_4$ *via* bio-organic compounds of *E. cognata*.

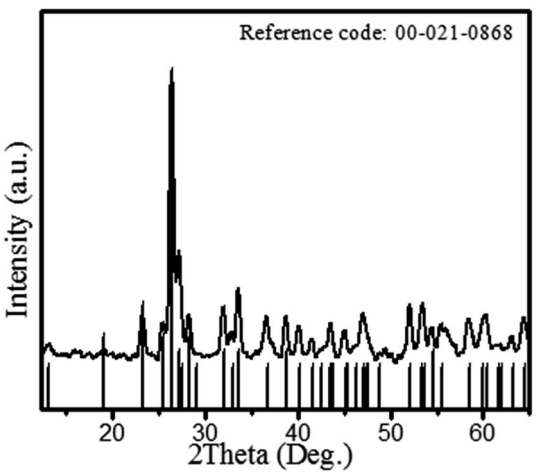

Fig. 3 XRD patterns of the $CoMoO_4$ nanomaterial.

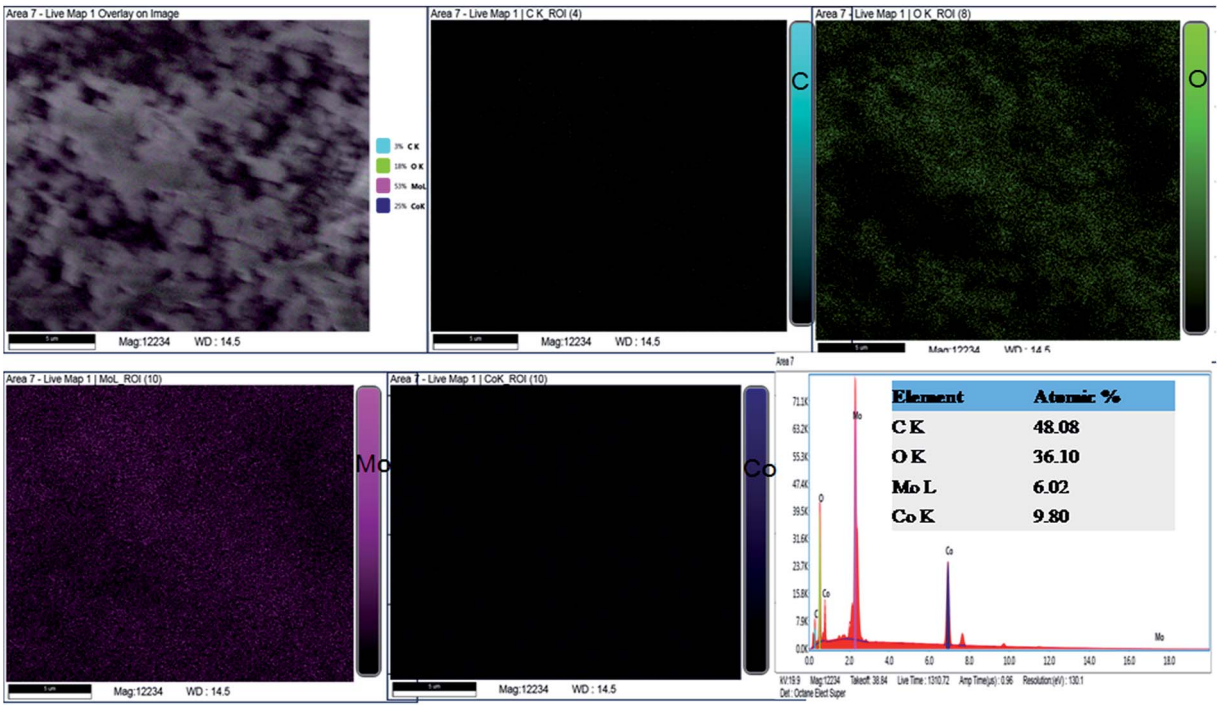

Fig. 4 Elemental analysis of the synthesized nanomaterial using energy dispersive X-ray spectroscopy.

Fig. 3 shows the XRD patterns of the bioorganic compound-derived $CoMoO_4$ nanomaterial. The diffraction patterns in Fig. 3 demonstrate well-defined prominent peaks at 2 theta (θ) = 13.2, 19.07, 23.30, 25.45, 26.42, 27.21, 28.32, 29.51, 32.02, 33.59, 36.66, 38.75, 40.13, 41.6, 43.54, 43.99, 45.07, 46.2, 47.05, 48.2, 52.09, 53.47, 54.04, 58.41, 60.42 and 64.35, corresponding to the (001), (−201), (021), (201), (002), (−112), (−311), (310), (−131), (022), (−222), (400), (040), (003), (222), (−422), (−223), (113), (−403), (241), (−133), (−204), (−440), (024), (−424) and (243) *hkl* planes, respectively. The peak patterns were exactly matched with $CoMoO_4$ of ICSD 00-021-0868. However, a minor shift (less than 0.1%) of the diffraction peaks towards lower diffraction angles was observed for some peaks. This indicates a compression of the crystal lattice due to the stress of organic stabilizing agents. The observed XRD patterns revealed the growth of monoclinic shape $CoMoO_4$ with a space group of $C2/m$ and cell parameters (Å) of a: 10.21, b: 9.268, c: 7.022. The crystallite size of $CoMoO_4$ was calculated from the full width half maximum (FWHM) of the peaks using the following Debye–Scherrer's equation:

$$D = (0.9 \times \lambda)/(\beta \cos \theta)$$

where λ = X-ray wavelength and β = full width at half maximum intensity of the peak (in Rad). The average particle size of cobalt molybdate was 23.5 nm. It is noted that no individual peak corresponding to Co, Co_3O_4, MoO_3, or Mo_3O_4 was found in Fig. 3. Therefore, the final product was $CoMoO_4$ as observed from the peaks pattern of XRD, which was confirmed by EDX (Fig. 4).

The EDX spectrum (Fig. 4) describes the chemical composition of the fabricated material to consist of Co, Mo, O and C. According to the atomic ratios of Co, Mo and O, the nanomaterial is classified as $CoMoO_4$. In agreement with the XRD phase analysis, EDX identified the synthesis of cobalt molybdate with a chemical formula of $CoMoO_4$. Nevertheless, the EDX study demonstrated the presence of a significant atomic percentage of carbon because of the organic functional groups of the stabilizing agents. Continuing with the investigation of the chemical composition, $CoMoO_4$ was subjected to XPS analysis to examine the local bonding environment of the synthesized material and to speculate the functional groups related to the bioactive compounds of *E. cognata*. The survey scan in Fig. 5a–d shows the composition of surface to be consistent with C, O, Co and Mo. The presence of Mo, Co, O_2 and C as major elements of the surface chemistry of the sample is in good agreement with the EDX analysis.

Continuing with the investigation of chemical composition, $CoMoO_4$ was subjected to XPS analysis to examine the surface composition of the synthesized material and to verify the presence of organic content of functional groups related to bioactive compounds of *E. cognata* at the surface. All spectra are calibrated on the binding energy scale relative to the C 1s hydrocarbon peak. The narrow XPS scans in Fig. 5(a–d) show the surface to contain C, O, Co and Mo in agreement with the EDX analysis.

The main Co $2p_{3/2}$ peak is rather broad and centred at a binding energy of 780.7, with a broad satellite feature at a binding energy (B.E.) of ~787 eV. The Co $2p_{3/2}$ peak is fitted with multiplet structure for Co^{2+} ions as detailed by Gupta and Sen[37] and Biesinger *et al.*[38] A reasonable agreement is obtained, suggesting the surface Co is mainly in the 2+ state. The

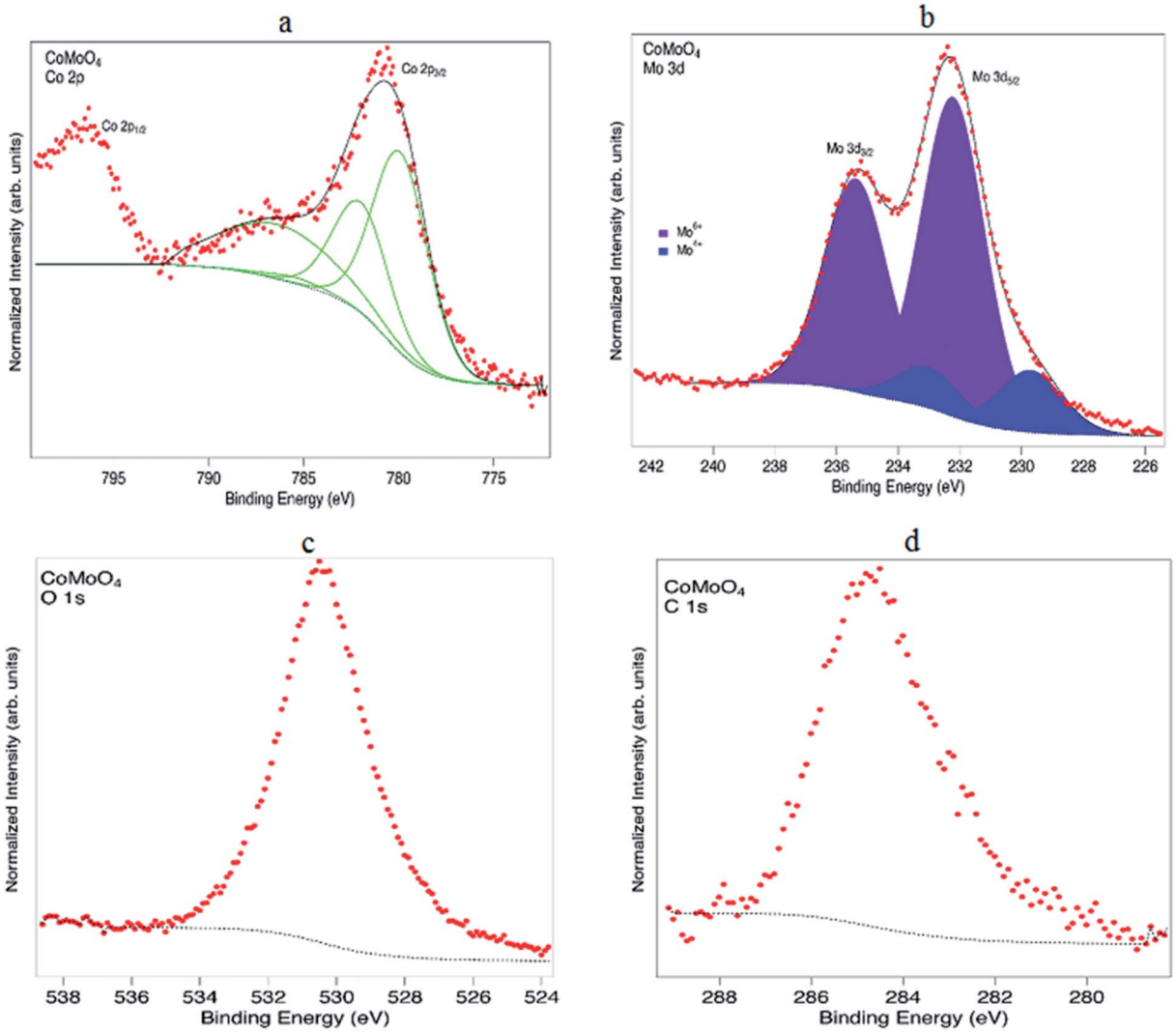

Fig. 5 (a) XPS spectra of Co 2p recorded from $CoMoO_4$, (b) spectra of Mo 3d, (c) XPS spectrum of O 1s and (d) spectrum of C 1s of $CoMoO_4$.

peak at 796.6 eV is the Co $2p_{1/2}$ peak which arises due to spin-orbit splitting.[38] Fig. 5b shows the Mo $3d_{5/2}$ and Mo $3d_{3/2}$ peaks centred at 232.3 and 235.4 eV, respectively.[61] These peaks must be fitted with two doublets at binding energies of 232.3 eV ($3d_{5/2}$) and 235.4 eV ($3d_{3/2}$) from Mo^{6+} in $CoMoO_4$ [43] and 229.7 eV ($3d_{5/2}$) and 233.1 eV ($3d_{3/2}$) from Mo^{4+}.[62] As for carbon and oxygen, for samples that have been exposed to air the information is often difficult to interpret. The C 1s peak at 284.8 eV is associated with C–C and C–H species, which may imply that there are compounds arising from the plant extract on the surface. Unfortunately due to some charging of the sample the region at higher binding energy where C–O species would lie was not recorded. The O 1s shows a main peak at an energy of ~530 eV, consistent with metal oxides.[42,44,63,64] However, as in the case of C, since the sample has been exposed to air there will also be contributions to the O 1s from water and hydroxide species.

FE-SEM images of the bioorganic-assisted $CoMoO_4$ are presented in Fig. 6a–c. The $CoMoO_4$ nanomaterial was examined at different magnifications with a well-defined nanostructure. It can be observed in Fig. 6 that at lower magnifications (10 and 5 μm), the spherical particles arranged themselves in quite uniform and regular structures. Thus, FE-SEM depicted the uniformly distributed spherical-shaped bioorganic-derived $CoMoO_4$ nanomaterials. In order to understand the effects of the bioactive compounds on the morphology of $CoMoO_4$, a blank experiment (also called the sol–gel experiment) was carried out involving citric acid ($C_6H_8O_7$) and ethylene glycol ($C_2H_6O_2$) in the ethanol (C_2H_5OH) solvent. All reducing and gelling agents in the control experiments were of synthetic analytic grade. The details of the controlled experiments are given in the ESI.† It can be observed that the chemical synthesis yielded microstructures (Figure 6d–f), which were larger in size than the organic template-assisted nanomaterial. The ethylene glycol-assisted particles had a nearly cuboidal shape, while the bio-templated particles were spherical in shape. Conversely, the chemically synthesized particles revealed less agglomeration, but with microstructures. The organic framework derived shows

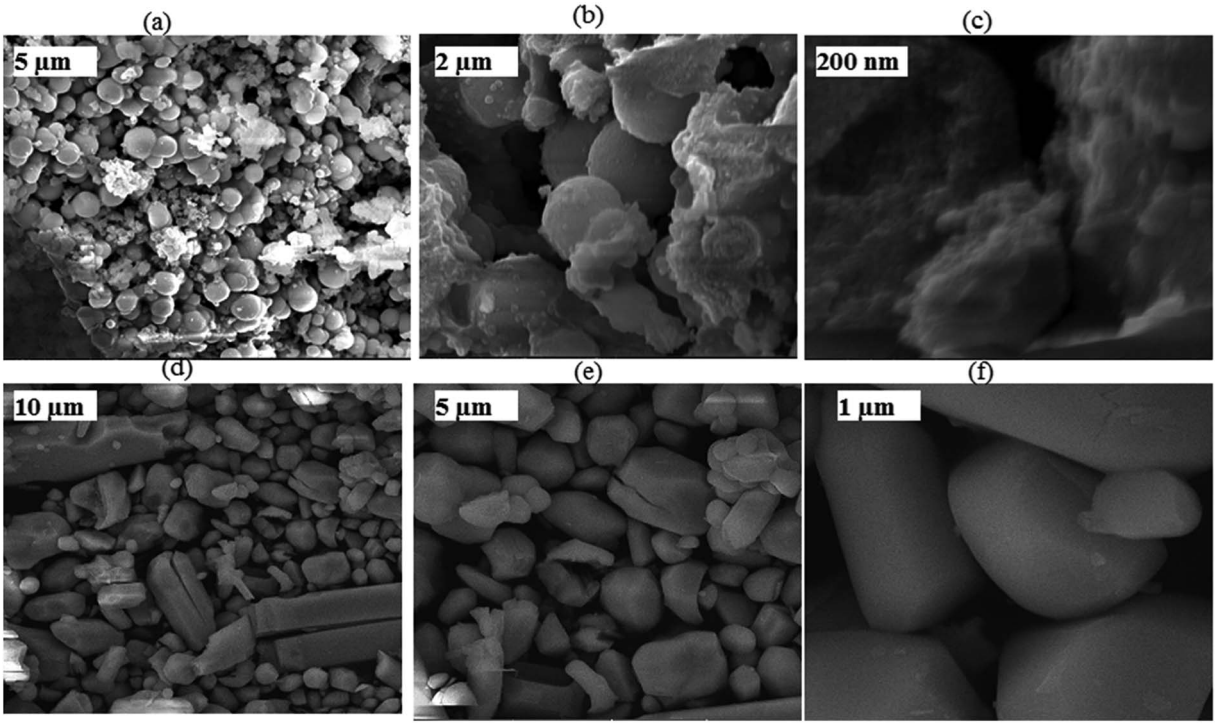

Fig. 6 (a–c) FE-SEM images of the organic template-assisted $CoMoO_4$ at different magnifications. (d–f) FE-SEM images of the controlled sample (ethylene glycol assisted $CoMoO_4$) at different magnifications.

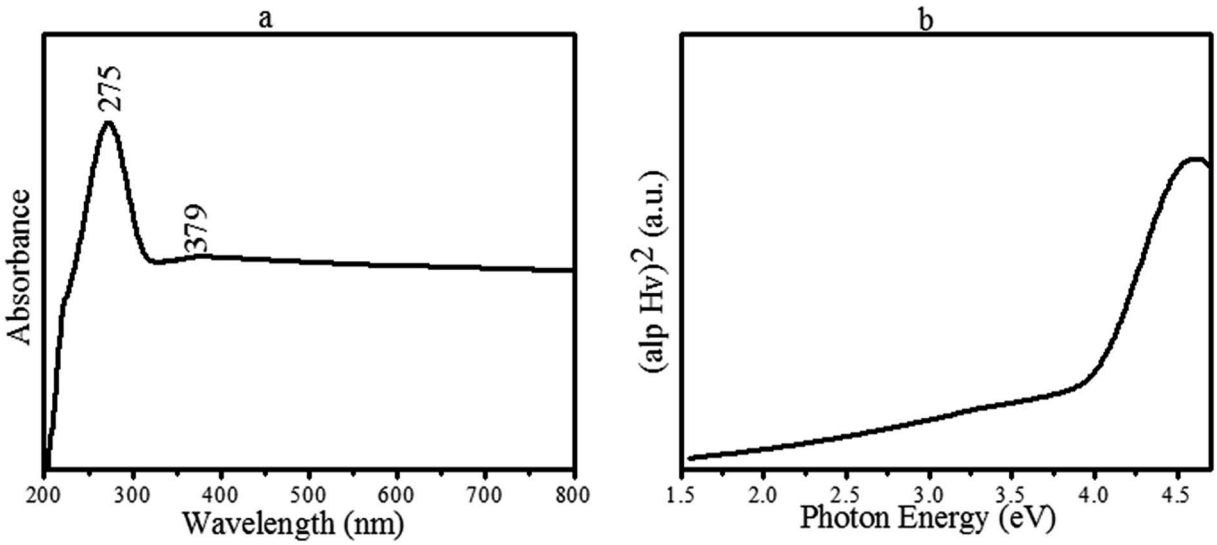

Fig. 7 (a) UV-Vis absorption spectra of $CoMoO_4$, and (b) band gap energy of $CoMoO_4$ *via* Tauc's plot.

little agglomeration at the nanoscale level. Therefore, the bio-template successfully synthesized nanoparticles, while the chemical synthesis yielded prominent microstructures. Moreover, from the present investigation and reported literature,[23–25] it was concluded that the phytochemicals of the leaves not only reduced the particle size but also prevented the agglomeration of the particles at the nanoscale.

4.2. Band gap energy

Fig. 7a shows the absorption spectrum of the fabricated $CoMoO_4$ metal oxides. From Fig. 6a, a wide-range absorption can be observed, which gradually increases towards the lower wavelength with a maximum absorption peak at 275 nm. The maximum absorption band indicates the presence of a blueshift due to the presence of Co oxide, which has a smaller band gap that absorbs the light in a blue shift. However, a small

absorption at 379 nm is also indicated in Fig. 7a. Fig. 7b represents the Tauc plot used to determine the optical band gap energy (E_g) of the synthesized material using the following relation:

$$(\alpha hv)^2 = A(hv - E_g)$$

where α is the absorption coefficient, and hv and E_g are defined as the photon and band gap energies, respectively. As seen in Fig. 7a, the band absorption edge of $CoMoO_4$ was found at 349 nm, corresponding to its band-gap excitation. However, the corresponding band gap energy was 3.6 eV for the synthesized $CoMoO_4$ composite from the Tauc plot.

5. Supercapacitive studies

The electrochemical properties of the organic compound-derived $CoMoO_4$ were characterized by CV, GCD and EIS. Fig. 8a shows typical voltammograms of the fabricated electrode at scan rates ranging from 2 to 300 mVs^{-1}. It is worth describing here that in agreement with the previous studies,[24,29,30] the Ni foam was just used as a mechanical support and current collector in the current investigation. It has no contribution to the capacitance of the electrode because of the negligible integrated area of the CV curves. However, the synthesized $CoMoO_4$ electrode revealed characteristics redox peaks, as shown in Fig. 8a. Li *et al.* reported that in the $CoMoO_4$ electrode, the Mo species are not involved in the redox reactions, as its role is to enhance the electrical conductivity of the electrode material. Therefore, according to the reported literature,[9–12,58] the emergence of the prominent redox peaks of the $CoMoO_4$ electrode are due to the faradaic reactions of M–O and/or M–OH (M = Co), as stated below:

$$3Co(OH)_2 + 2OH^- \leftrightarrow Co_3O_4 + 4H_2O + 2e^-$$

$$Co_3O_4 + H_2O + OH^- \leftrightarrow 3CoOOH + 2e^-$$

$$CoOOH + OH^- \leftrightarrow CoO_2 + H_2O + 2e^-$$

Moreover, the redox peaks also emerged due to the N-containing groups of the incorporated organic compounds

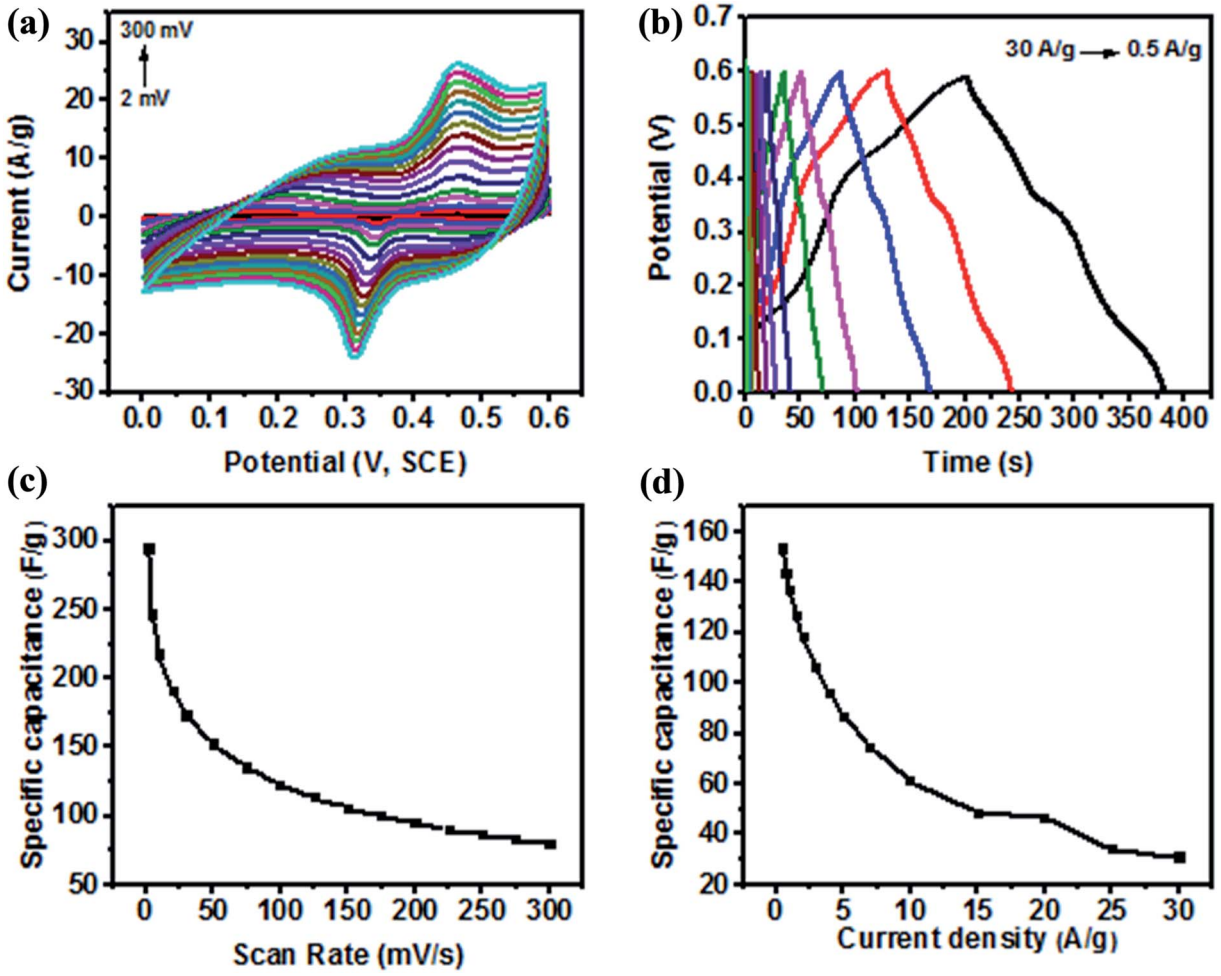

Fig. 8 (a) Cyclic voltammograms of the $CoMoO_4$ electrode at various scan rates. (b) Galvanostatic charge–discharge characteristics of $CoMoO_4$ at various current densities. (c) Variation of the specific capacitance as a function of the scan rate, and (d) variation of the specific capacitance as a function of the applied current density.

Table 2 Comparison of the supercapacitive behaviour of the fabricated nanomaterial with reported investigations by cyclic voltammetry

Electrode	Electrolyte	Specific capacitance (F g^{-1})	Scan rate (mV s^{-1})	References
$CoMoO_4$@C300	KNO_3	108.1	10	58
$ZnCo_2O_4$ nanowire	PVA/H_3PO_4	0.4 mF	100	46
Co_3O_4/CB	KOH	52	5	47
MoO_3-coated TiO_2 nanotubes with four MoO_3 deposition cycles	KCl	51.3	5 mV s^{-1}	68
MoO_3-coated TiO_2 nanotubes with 2 MoO_3 deposition cycles	KCl	44.9	5 mV s^{-1}	68
Co-doped TiO_2 NT/RGO	Na_2SO_4	34.8	5	49
Pure MoO_3	KCl	<10	5 mV s^{-1}	66
$CoMoO_4$	3 M KOH	294	2	Present work
		123	100	
		80.2	300	

($C_8H_{19}N$). The organic compounds are reported to have a huge reversible redox potential that makes them interesting candidates for pseudocapacitive energy storage,[36] particularly due to the introduction of nitrogen atoms. Pettong *et al.*,[17] Xie *et al.*[15] and Zhou *et al.*[78] reported in their studies that the introduction of nitrogen atoms greatly improved the pseudocapacitance behaviour of electrodes. In the current study, the redox peaks of $CoMoO_4$ were found to exhibit a direct positive correlation with the current density and scan rate. The oxidation reduction peaks were found to be increased with increasing current density and increasing the scan rate from 2 to 300 mV s^{-1}, as observed in Fig. 8a. The potentials of the redox peaks were shifted accordingly in more positive and negative directions with increasing scan rate, creating a wider potential difference ($E_c - E_a$) at higher potential, under quasi-reversible kinetics.[32,34,49,53] This is possibly attributed to the limited ion diffusion rate during the faradaic reactions to satisfy electronic neutralization at higher scan rates.[13,14,32] This behaviour of the electrode is associated with a typical battery-type electrode.[13,14,32,34] It is further noted that the separation between the redox peaks increased with increasing scan rate, indicating the fast faradaic reactions because of the spherical nanostructure of $CoMoO_4$. According to Zhang *et al.* and Bhagwan *et al.*, such redox behaviour is due to the ohmic resistance of the electrode.[4,41] Therefore, the cyclic voltammetry results indicated the functionalized $CoMoO_4$ as a pseudocapacitor that frequently relied on its redox behaviour as a battery-type electrode. This is because of the presence of Mo, Co, O_2, and C at the surface of the electrode as major constituents of the active material as shown by XPS in Fig. 3 and by EDX in Fig. 4. The battery-type behaviour is often associated with most metal oxides as reported by Duraisamy *et al.*, Wang *et al.*, and Hussain *et al.*, where they described such pseudocapacitive behaviours of metal oxide-based electrodes.[8,34,53] However, the fabricated $CoMoO_4$ electrode revealed an enhanced peak current density, as well as a larger increment of the integrated area than MoO_3,[66] MoO_2,[65] Co,[8] Co_3O_4,[18] and Co_3O_4/CoO[34] due to enhanced active sites provided by nanostructures, as well as O and C functional groups. The larger integrated area of the CV curve is significantly important as it reflects the capacitance of the electrode by the following relation:

$$C_{sp} = \frac{Q}{\Delta V \times \left(\frac{\partial v}{\partial t}\right) \times m}$$

where Q is the area under the CV curve, $\partial v/\partial t$ is the scan rate, ΔV is the potential window and m is the mass of the $CoMoO_4$ on the Ni electrode. As a result, greater the area under redox peaks, higher will be the capacitance.[1,29,30]

As shown in Fig. 8c, the fabricated electrode revealed a higher capacitance of 294 F g^{-1} at 2 mV s^{-1}, while the specific capacitance was observed to decrease with increasing scan rates because of the inaccessibility of the OH^- ions of the electrolyte to some parts of the electrode at higher scan rates. Despite this limitation of the electrolyte, a higher capacitance of 122 F g^{-1} and 80 F g^{-1} were still achievable at the maximum scan rates of 100 and 300 mV s^{-1}, respectively. This indicated the excellent rate capability (Fig. 8c) of $CoMoO_4$ because of a large number of active sites provided by Mo, Co and the functional groups of the organic species, as well as by spherical-shaped nanoparticles. The results of the present study is in agreement with the previous study of Altin *et al.*,[77] where they reported the favourable electrochemistry (considerable specific capacitance) of different ruthenium complexes with four different organic compounds. They reported that the specific capacitance of ruthenium was increased due to the higher surface areas of the organic compounds.

However, the specific capacitance calculated for $CoMoO_4$ in the current study (even at the highest rate of 300 mV s^{-1}) is much higher than the capacitance of 36 F g^{-1} of the MoO_3 nanorods,[66,67] 12 F g^{-1} of Co_3O_4,[47] 77 F g^{-1} of the commercial Co_3O_4 electrode,[18] and 60 F g^{-1} of the Co electrode[8] at the lowest scan rate of 5 mV s^{-1}. Moreover, Table 2 depicts a comparison of the capacitance of the $CoMoO_4$ electrode with previously reported electrodes. The comparison vividly demonstrates that the bioorganic compound-derived electrode revealed a much higher potential for the supercapacitor with an outstanding rate capability because of the combined effects of the surface

Table 3 Comparison of supercapacitive behaviour of $CoMoO_4$ nanomaterial with reported investigations *via* galvanostatic charge–discharge measurements

Electrode	Electrolyte	Specific capacitance (F g^{-1})	Current density (A g^{-1})	References
Co-doped TiO_2NT/RGO	Na_2SO_4	27.5	0.2	49
Mo-doped ZnO nanoflakes	KOH	46.2	10	50
$MnMoO_4$	NaOH	9.7	1	65
CoO/CNT	KOH	17.4	0.25	52
$CoMoO_4$	NaOH	62.8	1	65
MoO_3 nanowire	Na_2SO_4	23	0.5	69
$CoMoO_4$		153.2	0.5	Present
		97	5	work
		49	10	

chemistry and nanoscale morphology analyzed by XPS and FE-SEM, respectively.

The specific capacitance was further calculated from the charge–discharge curve (Fig. 8b) using the following equation:

$$C_{sp} = \frac{I \times \Delta t}{\Delta V \times m}$$

where I is the discharge current (A), Δt is the discharge time (s), ΔV is the potential window (V), and m is the mass (g) of the $CoMoO_4$ nanocomposites on the electrode. The capacitance of $CoMoO_4$ at various current densities was studied as shown in Fig. 8b and d. The GCD of the $CoMoO_4$ investigations revealed the highest capacitance of 153 F g^{-1} at 0.5 A g^{-1}, and the lowest capacitance of 31 F g^{-1} at the highest current density of 30 A g^{-1}. The calculated capacitance is much greater than the capacitance of 20 F g^{-1} of MoO_2,[70] 23 F g^{-1} of the MoO_3 nanowires,[69] and 17.9 F g^{-1} of Co/Co_3O_4 at a lower current density of 1 A g^{-1}.[56] In agreement with CV, the GCD measurements revealed an enhanced rate capability of $CoMoO_4$ due to increased active sites offered by organic compounds. The organic molecules as an electrode material revealed more reactive sites, thus revealing the redox stability that can provide a high specific capacity.[80] These results are consistent with those of Peng *et al.*,[80] Miroshnikov *et al.*,[79] and Xu *et al.*,[81] where it was reported that organic compounds (particularly having carbonyl and/or hydroxyl groups) are mostly derived from biomass, and mainly composed of C, H, O, and N elements, which were positively correlated with increasing capacitance, power and energy density. In another study, Fang *et al.* revealed the excellent specific capacitance (423 F g^{-1} at 0.5 A g^{-1}) of biomass (betel nut) derived doped carbon. Furthermore, Table 3 summarizes a comparison of the capacitance of the bioorganic framework-synthesized $CoMoO_4$ with previous investigations, and revealed the comparatively improved potential of the fabricated electrode for the supercapacitor. Therefore, in agreement with the literature,[1,29,30,55,69,70] the current investigations revealed the higher electrode capacitance at lower current densities and lower capacitance at higher current rates, which indicates a battery-type electrode. Moreover, the $CoMoO_4$ electrode revealed fast charge and discharge times because of the carbon-based organic stabilizing agents (C=O, C–H) in the sample as revealed by XPS. From Fig. 8b, it can be further observed that the area under the charging and discharging curve is larger at lower current densities and *vice versa*. This indicates the fast charging and discharging of $CoMoO_4$ at 30 A g^{-1}, and the slowest charging and discharging of the electrode at 0.5 A g^{-1}. Such inverse correlation between the charge–discharge time and the applied current density proposes that the insufficient faradaic reactions occur due to the poor utilization of the active mass at higher current density.[29–32]

Nevertheless, the presented results from the GCD measurements are in good agreement with the CV results; the fabricated electrode depicted pseudo-capacitance behaviour with outstanding redox peaks. To understand the conducting behaviour of the functionalized $CoMoO_4$-based electrodes, EIS measurements were performed for the estimation of the internal resistance and charge transfer resistance. The impedance results are shown in Fig. 9a–c. The Nyquist plot shown in Fig. 9b presented a semicircle arc in the low-frequency region (R_{ct}), and the intercept at the real part in the high frequency range stands for the internal resistance (R_i). Fig. 9a shows a line in the low frequency region called the Warburg element (Z_w).[1,29,30] It was observed in Fig. 9b that the organic-stabilized $CoMoO_4$ has a smaller intercept of 0.38 Ω at the real axis in the high frequency region. Thus, it has a smaller R_i that is due to the nanostructures, as well as the hydrophilic (oxygen) functional groups of the organic species on the surface, as revealed by XPS. The internal resistance of the $CoMoO_4$ electrodes is smaller than numerous fabricated metal oxide-based electrodes.[8–10,16,32,49] Moreover, Miroshnikov *et al.*[79] and Fang *et al.*[76] demonstrated outstanding capacitive behaviour by EIS analysis of organic compounds and biomass-carbon based electrodes, respectively, due to the C, H, N, and O atoms of the electrode material. Therefore, in the current study, the low internal resistance was strongly attributed to the fact that the pathways for electron transport were not only provided by Mo and Co, but also the organic stabilizing agents (C_4H_8O and $C_8H_{19}N$) of $CoMoO_4$ as indicated by XPS (Fig. 4) and MS spectra (Fig. 2b).

The fabricated electrode has a low charge-transfer resistance (R_{ct}) according to the semicircle arc in the high frequency region. This is due to the faradaic reactions of Co–Mo–O, as stated by Ujjain *et al.*, Xiao *et al.*, and Zequine *et al.*[16,32,49] Thus, R_{ct} confirms the enhanced pseudo-capacitance of the electrode. It can be further observed in the plot of Fig. 9a that there is a clear separation between the semicircle and vertical line of Z_w. The plot sharply increased in Fig. 9a and nearly became vertical (more close to 45°), corresponding to the Z-real axis indicating the smaller Warburg impedance. Therefore, the lower Z_w confirms the rapid diffusion of ions into the electrolyte and fast adsorption onto the electrode surface due to the surface chemistry and connected nanoparticles (Fig. 6) of $CoMoO_4$.

Fig. 9c presents the total impedance as a function of frequency. The total impedance of the electrode was observed to be decreased in the present investigation, which is consistent with Gervas *et al.* and Bhoyate *et al.*[29,30] Thus, the lower total

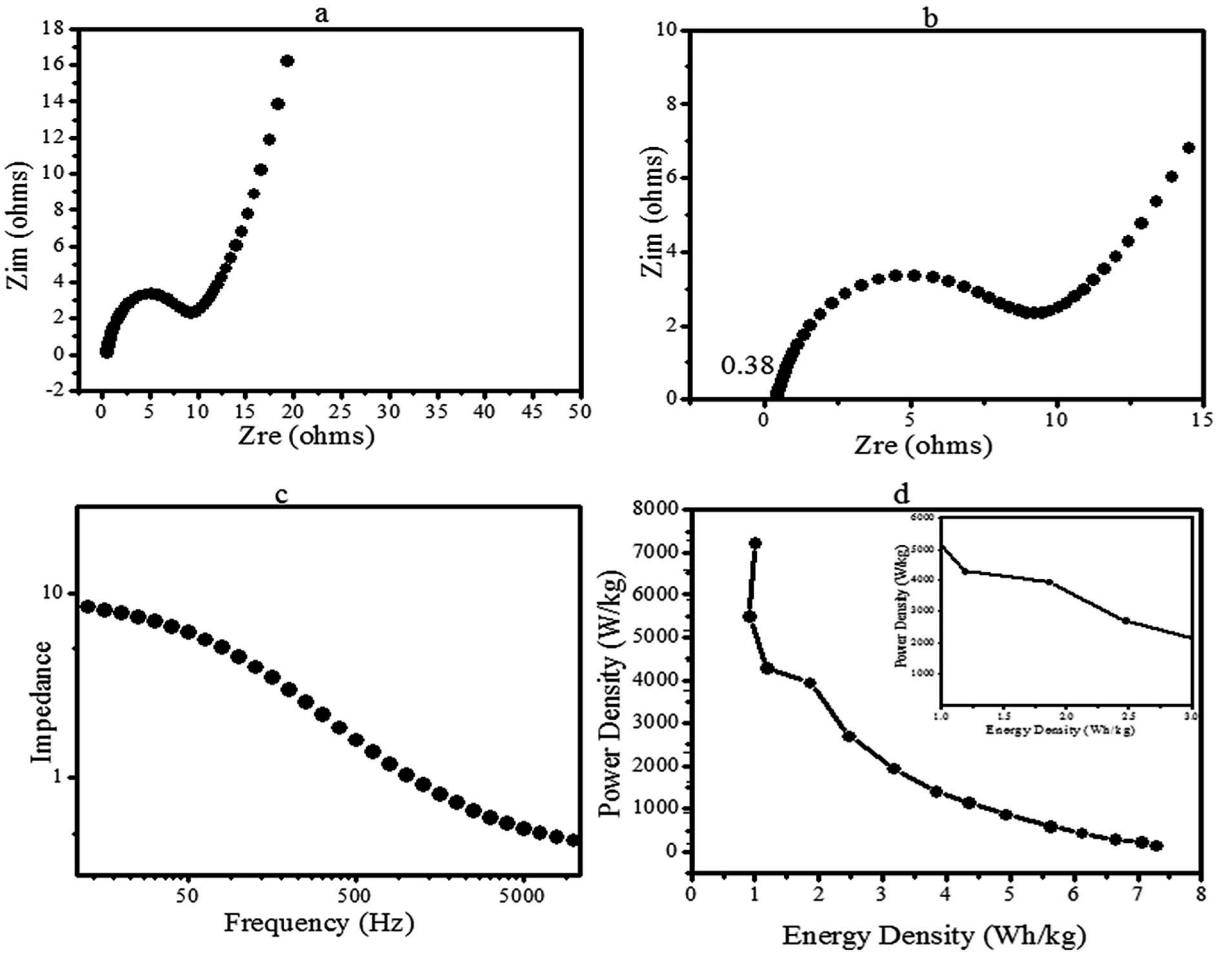

Fig. 9 (a) Nyquist plot of $CoMoO_4$ in the low frequency region, (b) Nyquist plot (semicircle arc) in the high-frequency region, (c) variation of impedance as a function of frequency, and (d) Ragone plot of $CoMoO_4$ (inset depicts the response of the energy density at higher power density).

impedance further designated the better conductive characteristics of $CoMoO_4$. These results indicated the good electrical conductivity of the fabricated electrode with faradaic reactions. Finally, the storage potential of the fabricated electrode was estimated by the energy density (E) and power density (P) using the discharge voltage *via* the following equations and are expressed as W h kg^{-1} and W kg^{-1}:

$$\text{Energy density}\,(E) = \frac{C \times \Delta V^2}{7.2}$$

$$\text{Power density}\,(P) = \frac{E \times 3600}{t}$$

where C (F g^{-1}) is the capacitance *via* galvanostatic charge discharge, ΔV (V) is the potential window and t (s) is the discharge time.[29,30,56] In the present study, the maximum calculated energy density of $CoMoO_4$ was 7.3 against a power density of 146, which is remarkably higher than the energy density of MoO_2, MoO_3,[66,69] Co–carbon (1.241 W h kg^{-1}), and Co_3O_4@Carbon (0.97 W h kg^{-1}).[56] The phytofabricated $CoMoO_4$ exhibited an enhanced energy storage potential in comparison with several reported devices.[39,40,49,56,65–70] On the other hand, the maximum recorded power density of $CoMoO_4$ was 7272.5 W kg^{-1} (7.3 kW kg^{-1}), which is much higher than the power densities of MoO_3,[66,70] Co_3O_4 nanorods,[57] CoO/Co_3O_4,[49] CoO nanofibers[56] and Co_3O_4@Carbon,[56] respectively. The Ragone plot (Fig. 9d) shows that when the power density increased, the energy density decreased and *vice versa*. A negative correlation between the energy density and powder density is a general phenomena associated with numerous other fabricated supercapacitors.[29–32] The inset in the Ragone plot (Fig. 9d inset) revealed the energy response of $CoMoO_4$ at the higher power densities. It is worth reporting that, in the current research, the energy density remained at 1.85 W h kg^{-1} at the higher power density of 4 kW kg^{-1}. This lower energy density of $CoMoO_4$ is still higher than the energy densities of Co@Carbon//Co@Carbon and Co_3O_4@Carbon//Co_3O_4@Carbon.[56] Consequently, in comparison with the previously reported investigation, the energy density and power density strongly suggested the potential of $CoMoO_4$ as an energy storage device.

Thus, in agreement with the low resistance, outstanding rate capability and efficient redox behaviour, the energy density and power density demonstrated the possibility of the fabricated $CoMoO_4$ electrode as a potential candidate for a supercapacitor.

6. Conclusion

Hereinto, we have successfully developed an inorganic–organic template for the synthesis of nanospherical-shaped cobalt molybdate using bioactive compounds of *E. cognata*. The obtained organic compound-assisted $CoMoO_4$ not only revealed the stabilization by octodrine and cyclobutanol, but also facilitated the enhanced electro-active sites for energy storage devices. $CoMoO_4$ demonstrated its efficient redox behaviour with a specific capacitance of almost 300 F g^{-1} in 3 M KOH aqueous solution. Furthermore, significant capacitance values of 123 and 61.2 F g^{-1} were still retained at a higher scan rate of 100 mV s^{-1} and current density of 10 A g^{-1}, respectively. Such excellent rate capability has been ascribed to the synergetic effects of the nanostructures and increased active sites created by C and O-related functional groups. In addition, the pathways provided by the hydrophilic functional oxygen groups of the organic stabilizing compounds, have reduced the resistance and enhanced diffusion/transport of electrons. Consequently, the considerable specific capacitance, good rate capability, and enhanced electrochemical conductivity promote the potential application of bioorganic compound-fabricated $CoMoO_4$ nanomaterials for supercapacitors.

Conflicts of interest

The authors declare that they have no known conflict of interest that would influence the work reported in this paper.

Acknowledgements

The authors acknowledge the Higher Education Commission of Pakistan, Department of Environmental Sciences, Fatima Jinnah Women University Rawalpindi Pakistan and the Department of Materials, Photon Science Institute and the Sir Henry Royce Institute, The University of Manchester U.K. The authors express their sincere acknowledgment to the Polymer Chemistry Program and the Kansas Polymer Research Center, Pittsburg State University for providing financial and research support to complete the electrochemical part of this project.

References

1 L. Fu, Q. Qu, R. Holze, V. V. Kondratiev and Y. Wu, Composites of metal oxides and intrinsically conducting polymers as supercapacitor electrodes: The best of both worlds?, *J. Mater. Chem. A*, 2019, 7, 14937–14970.

2 S. Lichušina, L. Staišiūnas, V. Jasulaitienė, A. Selskis and K. Leinartas, Capacitive properties, structure, and composition of porous Co hydroxide/oxide layers formed by dealloying of Zn–Co alloy, *J. Appl. Electrochem.*, 2019, **49**(5), 503–515.

3 W. Su, R. Miao, B. Tao and F. Miao, High-performance symmetric supercapacitor based on flower-like zinc-cobalt-molybdenum hybrid metal oxide, *Ionics*, 2019, 1–9.

4 J. Bhagwan, G. Nagaraju, B. Ramulu and J. S. Yu, Promotive Effect of MWCNT on ZnCo2O4 Hexagonal Plates and Their Application in Aqueous Asymmetric Supercapacitor, *J. Electrochem. Soc.*, 2019, **166**(2), A217–A224.

5 A. Ali, M. Ammar, M. Ali, Z. Yahya, M. Y. Javaid, S. ul Hassan and T. Ahmed, Mo-doped ZnO nanoflakes on Ni-foam for asymmetric supercapacitor applications, *RSC Adv.*, 2019, **9**(47), 27432–27438.

6 I. Shakir, M. Shahid, S. Cherevko, C. H. Chung and D. J. Kang, Ultrahigh-energy and stable supercapacitors based on intertwined porous MoO_3–MWCNT nanocomposites, *Electrochim. Acta*, 2011, **58**, 76–80.

7 Q. Zhang, Z. Liu, B. Zhao, Y. Cheng, L. Zhang, H. H. Wu, Y. Wu, *et al.*, Design and understanding of dendritic mixed-metal hydroxide nanosheets@ N-doped carbon nanotube array electrode for high-performance asymmetric supercapacitors, *Energy Storage Materials*, 2019, **1**(6), 632–645.

8 I. Hussain, S. G. Mohamed, A. Ali, N. Abbas, S. M. Ammar and W. Al Zoubi, Uniform growth of Zn-Mn-Co ternary oxide nanoneedles for high-performance energy-storage applications, *J. Electroanal. Chem.*, 2019, **837**, 39–47.

9 D. Kong, Y. Wang, S. Huang, J. Hu, Y. Von Lim, B. Liu, H. Y. Yang, *et al.*, 3D self-branched zinc-cobalt Oxide@ N-doped carbon hollow nanowall arrays for high-performance asymmetric supercapacitors and oxygen electrocatalysis, *Energy Storage Materials*, 2019, **23**, 653–663.

10 C. Chen, S. Wang, X. Luo, W. Gao, G. Huang, Y. Zeng and Z. Zhu, Reduced $ZnCo_2O_4$@ $NiMoO_4.H_2O$ heterostructure electrodes with modulating oxygen vacancies for enhanced aqueous asymmetric supercapacitors, *J. Power Sources*, 2019, **409**, 112–122.

11 Y. Liu, X. Cao, L. Cui, Y. Zhong, R. Zheng, D. Wei, J. Liu, *et al.*, Zn-Ni-Co trimetallic carbonate hydroxide nanothorns branched on $Cu(OH)_2$ nanorods array based on Cu foam for high-performance asymmetric supercapacitors, *J. Power Sources*, 2019, **437**, 226897.

12 Y. Yang, Y. Zhou, Z. Hu, W. Wang, X. Zhang, L. Qiang and Q. Wang, 3D thin-wall cell structure nickel-cobalt-molybdenum ternary phosphides on carbon cloth as high-performance electrodes for asymmetric supercapacitors, *J. Alloys Compd.*, 2019, **772**, 683–692.

13 Z. Xu, T. Wang, L. Wang, J. Xu, P. Liu, X. Lan, F. Jiang, *et al.*, Aniline-grafting graphene oxide/polyaniline composite prepared via interfacial polymerization with high capacitive performance, *Int. J. Energy Res.*, 2019, **43**(13), 7693–7701.

14 K. D. Poopalam, L. Raghunanan, L. Bouzidi, S. K. Yeong and S. S. Narine, Lipid-derived monoamide as phase change energy storage materials, *Int. J. Energy Res.*, 2019, **43**(13), 6934–6950.

15 F. Xie, M. Zhou, G. Wang, Q. Wang, M. Yan and H. Bi, Morphology-dependent electrochemical performance of nitrogen-doped carbon dots@polyaniline hybrids for supercapacitors, *Int. J. Energy Res.*, 2019, **43**(13), 7529–7540.

16 S. K. Ujjain, G. Singh and R. K. Sharma, Co_3O_4@ reduced graphene oxide nanoribbon for high performance asymmetric supercapacitor, *Electrochim. Acta*, 2015, **169**, 276–282.

17 T. Pettong, P. Iamprasertkun, A. Krittayavathananon, P. Sukha, P. Sirisinudomkit, A. Seubsai, M. Sawangphruk, *et al.*, High-performance asymmetric supercapacitors of $MnCo_2O_4$ nanofibers and N-doped reduced graphene oxide aerogel, *ACS Appl. Mater. Interfaces*, 2016, **8**(49), 34045–34053.

18 W. Du, R. Liu, Y. Jiang, Q. Lu, Y. Fan and F. Gao, Facile synthesis of hollow Co_3O_4 boxes for high capacity supercapacitor, *J. Power Sources*, 2013, **227**, 101–105.

19 S. Wu, J. Liu, H. Wang and H. Yan, A review of performance optimization of MOF-derived metal oxide as electrode materials for supercapacitors, *Int. J. Energy Res.*, 2019, **43**(2), 697–716.

20 J. Yu, X. Gao, Z. Cui, Y. Jiao, Q. Zhang, H. Dong, L. Dong, *et al.*, Facile Synthesis of Binary Transition Metal Sulfide Tubes Derived from NiCo-MOF-74 for High-Performance Supercapacitors, *Energy Technol.*, 2019, **7**(6), 1900018.

21 H. A. Abdelgadir and J. Van Staden, Ethnobotany, ethnopharmacology and toxicity of *Jatropha curcas* L. (Euphorbiaceae): A review, *S. Afr. J. Bot.*, 2013, **88**, 204–218.

22 S. Mondal, D. Ghosh and K. Ramakrishna, A complete profile on blind-your-eye mangrove *Excoecaria agallocha* L. (Euphorbiaceae): Ethnobotany, phytochemistry, and pharmacological aspects, *Pharmacogn. Rev.*, 2016, **10**(20), 123.

23 W. R. Rolim, M. T. Pelegrino, B. de Araújo Lima, L. S. Ferraz, F. N. Costa, J. S. Bernardes, A. B. Seabra, *et al.*, Green tea extract mediated biogenic synthesis of silver nanoparticles: characterization, cytotoxicity evaluation and antibacterial activity, *Appl. Surf. Sci.*, 2019, **463**, 66–74.

24 A. Hussain, M. Oves, M. F. Alajmi, I. Hussain, S. Amir, J. Ahmed, I. Ali, *et al.*, Biogenesis of ZnO nanoparticles using *Pandanus odorifer* leaf extract: anticancer and antimicrobial activities, *RSC Adv.*, 2019, **9**(27), 15357–15369.

25 A. Shelar, J. Sangshetti, S. Chakraborti, A. V. Singh, R. Patil and S. Gosavi, Helminthicidal and Larvicidal Potentials of Biogenic Silver Nanoparticles Synthesized from Medicinal Plant *Momordica charantia*, *Med. Chem.*, 2019, **15**(7), 781–789.

26 S. B. Jaffri and K. S. Ahmad, Augmented photocatalytic, antibacterial and antifungal activity of prunosynthetic silver nanoparticles, *Artif. Cells, Nanomed., Biotechnol.*, 2018, **46**(1), 127–137.

27 J. P. Mehta, T. Tian, Z. Zeng, G. Divitini, B. M. Connolly, P. A. Midgley, A. E. Wheatley, *et al.*, Sol–Gel synthesis of robust metal–organic frameworks for nanoparticle encapsulation, *Adv. Funct. Mater.*, 2018, **28**(8), 1705588.

28 D. Gnanasangeetha and D. S. Thambavani, One pot synthesis of zinc oxide nanoparticles via chemical and green method, *Res. J. Mater. Sci.*, 2013, **2320**, 6055.

29 C. Gervas, M. D. Khan, S. Mlowe, C. Zhang, C. Zhao, R. K. Gupta, N. Revaprasadu, *et al.*, Synthesis of Off-Stoichiometric CoS Nanoplates from a Molecular Precursor for Efficient H2/O2 Evolution and Supercapacitance, *ChemElectroChem*, 2019, **6**(9), 2560–2569.

30 S. Bhoyate, P. K. Kahol, B. Sapkota, S. R. Mishra, F. Perez and R. K. Gupta, Polystyrene activated linear tube carbon nanofiber for durable and high-performance supercapacitors, *Surf. Coat. Technol.*, 2018, **345**, 113–122.

31 S. Palchoudhury, K. Ramasamy, R. K. Gupta and A. Gupta, Flexible Supercapacitors: A Materials Perspective, *Front. Mater.*, 2019, **5**, 83.

32 C. Zequine, S. Bhoyate, F. Wang, X. Li, K. Siam, P. K. Kahol and R. K. Gupta, Effect of solvent for tailoring the nanomorphology of multinary CuCo2S4 for overall water splitting and energy storage, *J. Alloys Compd.*, 2019, **784**, 1–7.

33 J. L. Aleixandre-Tudo and W. Du Toit, The Role of UV-Visible Spectroscopy for Phenolic Compounds Quantification in Winemaking, in *Frontiers and New Trends in the Science of Fermented Food and Beverages*, IntechOpen, 2018, DOI: 10.5772/intechopen.79550.

34 E. Duraisamy, H. T. Das, A. S. Sharma and P. Elumalai, Supercapacitor and photocatalytic performances of hydrothermally-derived Co_3O_4/CoO@ carbon nanocomposite, *New J. Chem.*, 2018, **42**(8), 6114–6124.

35 A. Pramanik, S. Maiti, M. Sreemany and S. Mahanty, High electrochemical energy storage in self-assembled nest-like CoO nanofibers with long cycle life, *J. Nanopart. Res.*, 2016, **18**(4), 93.

36 A. Borenstein, O. Hanna, R. Attias, S. Luski, T. Brousse and D. Aurbach, Carbon-based composite materials for supercapacitor electrodes: a review, *J. Mater. Chem. A*, 2017, **5**(25), 12653–12672.

37 R. P. Gupta and S. K. Sen, Calculation of multiplet structure of core p-vacancy levels, *Phys. Rev. B: Solid State*, 1974, **10**(1), 71–77.

38 M. C. Biesinger, B. P. Payne, A. P. Grosvenor, L. W. Lau, A. R. Gerson and R. S. C. Smart, Resolving surface chemical states in XPS analysis of first row transition metals, oxides and hydroxides: Cr, Mn, Fe, Co and Ni, *Appl. Surf. Sci.*, 2011, **257**(7), 2717–2730.

39 M. S. Yadav, A. K. Sinha and M. N. Singh, Electrochemical behaviour of ZnO–AC based nanocomposite electrode for supercapacitor, *Mater. Res. Express*, 2018, **5**(8), 085503.

40 M. S. Yadav, N. Singh and A. Kumar, Synthesis and characterization of zinc oxide nanoparticles and activated charcoal based nanocomposite for supercapacitor electrode application, *J. Mater. Sci.: Mater. Electron.*, 2018, **29**(8), 6853–6869.

41 C. Zhang, S. Bhoyate, C. Zhao, P. K. Kahol, N. Kostoglou, C. Mitterer, C. Rebholz, *et al.*, Electrodeposited Nanostructured CoFe2O4 for Overall Water Splitting and Supercapacitor Applications, *Catalysts*, 2019, **9**(2), 176.

42 S. Oswald, Binding energy referencing for XPS in alkali metal-based battery materials research (I): basic model investigations, *Appl. Surf. Sci.*, 2015, **351**, 492–503.

43 N. S. McIntyre, D. D. Johnston, L. L. Coatsworth, R. D. Davidson and J. R. Brown, X-ray photoelectron spectroscopic studies of thin film oxides of cobalt and molybdenum, *Surf. Interface Anal.*, 1990, **15**(4), 265–272.

44 R. Lindsay and G. Thornton, Probing well-characterized metal oxide surfaces with synchrotron radiation, *J. Phys.: Condens. Matter*, 2001, **13**(49), 11.

45 H. Wu, Z. Lou, H. Yang and G. Shen, A flexible spiral-type supercapacitor based on ZnCo 2 O 4 nanorod electrodes, *Nanoscale*, 2015, **7**(5), 1921–1926.

46 B. Liu, D. Tan, X. Wang, D. Chen and G. Shen, Flexible, Planar-Integrated, All-Solid-State Fiber Supercapacitors with an Enhanced Distributed-Capacitance Effect, *Small*, 2013, **9**(11), 1998–2004.

47 W. Zhou, J. Liu, T. Chen, K. S. Tan, X. Jia, Z. Luo, T. Yu, *et al.*, Fabrication of Co_3O_4-reduced graphene oxide scrolls for high-performance supercapacitor electrodes, *Phys. Chem. Chem. Phys.*, 2011, **13**(32), 14462–14465.

48 L. S. Aravinda, K. K. Nagaraja, H. S. Nagaraja, K. U. Bhat and B. R. Bhat, ZnO/carbon nanotube nanocomposite for high energy density supercapacitors, *Electrochim. Acta*, 2013, **95**, 119–124.

49 H. Xiao, W. Guo, B. Sun, M. Pei and G. Zhou, Mesoporous TiO_2 and Co-doped TiO_2 nanotubes/reduced graphene oxide composites as electrodes for supercapacitors, *Electrochim. Acta*, 2016, **190**, 104–117.

50 A. Ali, M. Ammar, M. Ali, Z. Yahya, M. Y. Javaid, S. ul Hassan and T. Ahmed, Mo-doped ZnO nanoflakes on Ni-foam for asymmetric supercapacitor applications, *RSC Adv.*, 2019, **9**(47), 27432–27438.

51 J. S. Suroshe and S. S. Garje, Capacitive behaviour of functionalized carbon nanotube/ZnO composites coated on a glassy carbon electrode, *J. Mater. Chem. A*, 2015, **3**(30), 15650–15660.

52 Y. G. Zhu, Y. Wang, Y. Shi, J. I. Wong and H. Y. Yang, CoO nanoflowers woven by CNT network for high energy density flexible micro-supercapacitor, *Nano Energy*, 2014, **3**, 46–54.

53 H. Wang, C. Shen, J. Liu, W. Zhang and S. Yao, Three-dimensional $MnCo_2O_4$/graphene composites for supercapacitor with promising electrochemical properties, *J. Alloys Compd.*, 2019, **792**, 122–129.

54 Z. Li, Z. Zhou, G. Yun, K. Shi, X. Lv and B. Yang, High-performance solid-state supercapacitors based on graphene-ZnO hybrid nanocomposites, *Nanoscale Res. Lett.*, 2013, **8**(1), 473.

55 K. Subramani and M. Sathish, Facile synthesis of ZnO nanoflowers/reduced graphene oxide nanocomposite using zinc hexacyanoferrate for supercapacitor applications, *Mater. Lett.*, 2019, **236**, 424–427.

56 E. Dai, J. Xu, J. Qiu, S. Liu, P. Chen and Y. Liu, Co@ Carbon and Co3O4@ Carbon nanocomposites derived from a single MOF for supercapacitors, *Sci. Rep.*, 2017, **7**(1), 12588.

57 T. Meng, Q. Q. Xu, Z. H. Wang, Y. T. Li, Z. M. Gao, X. Y. Xing and T. Z. Ren, Co_3O_4 nanorods with self-assembled nanoparticles in queue for supercapacitor, *Electrochim. Acta*, 2015, **180**, 104–111.

58 J. Li, C. Zhao, Y. Yang, C. Li, T. Hollenkamp, N. Burke, W. Chen, *et al.*, Synthesis of monodispersed $CoMoO_4$ nanoclusters on the ordered mesoporous carbons for environment-friendly supercapacitors, *J. Alloys Compd.*, 2019, **810**, 151841.

59 T. Prabhakaran and J. Hemalatha, Chemical control on the size and properties of nano NiFe2O4 synthesized by sol–gel autocombustion method, *Ceram. Int.*, 2014, **40**(2), 3315–3324.

60 C. C. Vidyasagar, Y. A. Naik, T. G. Venkatesha and P. Manjunatha, Sol–gel synthesis using glacial acetic acid and optical properties of anatase Cu–TiO2 nanoparticles, *J. Nanoeng. Nanomanuf.*, 2012, **2**(1), 91–98.

61 A. Habibi-Yangjeh, M. Mousavi and K. Nakata, Boosting visible-light photocatalytic performance of g-C3N4/Fe3O4 anchored with $CoMoO_4$ nanoparticles: novel magnetically recoverable photocatalysts, *J. Photochem. Photobiol., A*, 2019, **368**, 120–136.

62 P. C. Kao, C. J. Hsieh, Z. H. Chen and S. H. Chen, Improvement of MoO3/Ag/MoO_3 multilayer transparent electrodes for organic solar cells by using UV–ozone treated MoO_3 layer, *Sol. Energy Mater. Sol. Cells*, 2018, **186**, 131–141.

63 M. Abu-Samha, K. J. Børve, M. Winkler, J. Harnes, L. J. Saethre, A. Lindblad, S. Svensson, *et al.*, The local structure of small water clusters: imprints on the core-level photoelectron spectrum, *J. Phys. B: At., Mol. Opt. Phys.*, 2009, **42**(6), 069801.

64 A. Furlan, J. Lu, L. Hultman, U. Jansson and M. Magnuson, Crystallization characteristics and chemical bonding properties of nickel carbide thin film nanocomposites, *J. Phys.: Condens. Matter*, 2014, **26**(41), 415501.

65 L. Q. Mai, F. Yang, Y. L. Zhao, X. Xu, L. Xu and Y. Z. Luo, Hierarchical MnMoO 4/CoMoO 4 heterostructured nanowires with enhanced supercapacitor performance, *Nat. Commun.*, 2011, **2**, 381.

66 T. Tao, Q. Chen, H. Hu and Y. Chen, MoO_3 nanoparticles distributed uniformly in carbon matrix for supercapacitor applications, *Mater. Lett.*, 2012, **66**(1), 102–105.

67 W. Q. Tang, J. Y. Xu and Z. Y. Gu, Metal–Organic-Framework-based Gas Chromatographic Separation, *Chem.–Asian J.*, 2019, **14**(20), 3462–3473.

68 D. Guan, X. Gao, J. Li and C. Yuan, Enhanced capacitive performance of TiO2 nanotubes with molybdenum oxide coating, *Appl. Surf. Sci.*, 2014, **300**, 165–170.

69 I. Shakir, M. Shahid, S. Cherevko, C. H. Chung and D. J. Kang, Ultrahigh-energy and stable supercapacitors based on intertwined porous MoO_3–MWCNT nanocomposites, *Electrochim. Acta*, 2011, **58**, 76–80.

70 W. Shaheen, M. F. Warsi, M. Shahid, M. A. Khan, M. Asghar, Z. Ali, I. Shakir, *et al.*, Carbon coated MoO_3 nanowires/graphene oxide ternary nanocomposite for high-performance supercapacitors, *Electrochim. Acta*, 2016, **219**, 330–338.

71 L. Chauhan, A. K. Shukla and K. Sreenivas, Dielectric and magnetic properties of Nickel ferrite ceramics using crystalline powders derived from DL alanine fuel in sol–gel auto-combustion, *Ceram. Int.*, 2015, **41**(7), 8341–8351.

72 V. Catalani, M. Prilutskaya, A. Al-Imam, S. Marrinan, Y. Elgharably, M. Zloh, O. Corazza, *et al.*, Octodrine: new questions and challenges in sport supplements, *Brain Sci.*, 2018, **8**(2), 34.

73 P. A. Cohen, J. C. Travis, P. H. Keizers, P. Deuster and B. J. Venhuis, Four experimental stimulants found in

sports and weight loss supplements: 2-amino-6-methylheptane (octodrine), 1, 4-dimethylamylamine (1, 4-DMAA), 1, 3-dimethylamylamine (1, 3-DMAA) and 1, 3-dimethylbutylamine (1, 3-DMBA), *Clin. Toxicol.*, 2018, **56**(6), 421–426.

74 P. Y. Mali and S. S. Panchal, *Euphorbia neriifolia* L.: Review on botany, ethnomedicinal uses, phytochemistry and biological activities, *Asian Pac. J. Trop. Med.*, 2017, **10**(5), 430–438.

75 S. Mondal, D. Ghosh and K. Ramakrishna, A complete profile on blind-your-eye mangrove *Excoecaria agallocha* L. (Euphorbiaceae): ethnobotany, phytochemistry, and pharmacological aspects, *Pharmacogn. Rev.*, 2016, **10**(20), 123.

76 J. Fang, D. Guo, C. Kang, S. Wan, S. Li, L. Fu, Q. Liu, *et al.*, Enhanced hetero-elements doping content in biomass waste-derived carbon for high performance supercapacitor, *Int. J. Energy Res.*, 2019, **43**(14), 8811–8821.

77 S. Altin, E. Öz, S. Altundağ, A. Bayri, T. Roisnel, V. Dorcet, S. Yaşar, *et al.*, Investigation of hybrid-capacitor properties of ruthenium complexes, *Int. J. Energy Res.*, 2019, **43**(13), 6840–6851.

78 C. Zhou, X. Yan, J. Wang, X. Yuan, D. Wang, Y. Zhu and X. Cheng, Mn3O4 nanoparticles on activated carbonitride by soft chemical method for symmetric coin cell supercapacitors, *Int. J. Energy Res.*, 2019, **43**(14), 8481–8491.

79 M. Miroshnikov, K. Kato, G. Babu, K. P. Divya, L. M. R. Arava, P. M. Ajayan and G. John, A common tattoo chemical for energy storage: henna plant-derived naphthoquinone dimer as a green and sustainable cathode material for Li-ion batteries, *RSC Adv.*, 2018, **8**(3), 1576–1582.

80 H. Peng, Q. Yu, S. Wang, J. Kim, A. E. Rowan, A. K. Nanjundan, J. Yu, *et al.*, Molecular design strategies for electrochemical behavior of aromatic carbonyl compounds in organic and aqueous electrolytes, *Adv. Sci.*, 2019, **6**(17), 1900431.

81 Y. Xu, M. Zhou and Y. Lei, Organic materials for rechargeable sodium-ion batteries, *Mater. Today*, 2018, **21**(1), 60–78.